

Analysis of Wave Behavior in Lossy Dielectric Samples at High Field

Qing X. Yang,^{1*} Jinghua Wang,¹ Xiaoliang Zhang,² Christopher M. Collins,¹ Michael B. Smith,¹ Haiying Liu,² Xiao-Hong Zhu,² J. Thomas Vaughan,¹ Kamil Ugurbil,² and Wei Chen²

Radiofrequency (RF) field wave behavior and associated non-uniform image intensity at high magnetic field strengths are examined experimentally and numerically. The RF field produced by a 10-cm-diameter surface coil at 300 MHz is evaluated in a 16-cm-diameter spherical phantom with variable salinity, and in the human head. Temporal progression of the RF field indicates that the standing wave and associated dielectric resonance occurring in a pure water phantom near 300 MHz is greatly dampened in the human head due to the strong decay of the electromagnetic wave. The characteristic image intensity distribution in the human head is the result of spatial phase distribution and amplitude modulation by the interference of the RF traveling waves determined by a given sample-coil configuration. The numerical calculation method is validated with experimental results. The general behavior of the RF field with respect to the average brain electrical properties in a frequency range of 42–350 MHz is also analyzed. Magn Reson Med 47: 982–989, 2002. © 2002 Wiley-Liss, Inc.

Key words: calculations; B_1 ; high field; MRI; radiofrequency

Enhancements in signal-to-noise ratio (SNR) and T_2^* contrast arising from high static magnetic field strengths are desirable for in vivo MR applications. Thus, the number of high-field human MRI systems has increased rapidly in recent years (1–10). The advent of high-field human imaging systems introduces new challenges in radiofrequency (RF) engineering (11,12). Because at high frequencies the wavelength of the RF field is comparable to or less than that of the dimension of the human body, the RF magnetic field (B_1) inside a sample exhibits prominent wave behavior (13–16). Additionally, the homogeneity of the B_1 field and source currents in the RF coil are strongly perturbed by sample loading (17–19). The B_1 field distribution inside a sample is important for both specific absorption rate (SAR) assessment and RF coil engineering at high frequency. However, mathematical treatment of the RF field in such systems can be extremely complicated because 1) the quasi-static approximations are no longer valid, and Maxwell's wave equation must be employed; and 2) the geometry of the human body is irregular, and electromagnetic

properties of tissues are heterogeneous. Thus, computer numerical calculation becomes an effective and indispensable tool for studying interactions of the RF field with the human body at high field (20–24). Associated with the RF field wave behavior, the distributions of the B_1 field and its circularly polarized components B^+ and B^- , which are directly responsible for the MR image intensity distribution, become distinctively different from one another. Consequently, the relationship of RF field polarization to coil configuration and sample electric properties needs to be analyzed in order to understand the resultant image intensity distribution. Computer modeling provides an effective way to study this problem, and may provide insight into complex RF field wave behavior and its dependence on the electrical properties of the sample. In this report, we present a study specifically devised to analyze high-frequency wave behavior of the RF field with the aid of numerical calculation and parallel experimental measurements.

METHODS

The study was carried out using water and saline phantoms with a 10-cm-diameter surface coil made from copper foil (Fig. 1). The phantoms consisted of 16-cm-diameter spherical bottles filled with either deionized water or saline solution. The water phantom exhibits a strong, two-lobe dielectric resonance at approximately the Larmor frequency. Conductivity (σ) of the phantom was adjusted by changing the saline concentration. Computer models of the experimental phantom were generated on a rectilinear grid with 2-mm resolution in each dimension. The region for calculation of the phantom model was defined as a $34 \times 34 \times 24$ cm rectangular space in the x , y , and z directions. The sample was assigned a relative electric permittivity (ϵ_r) of 78, and conductivities (σ) of 0.0, 0.26, 0.67, and 1.9 S/m corresponding to 0.0, 20, 50, and 150 mM salinity, respectively. The conductivity value 0.67 S/m is hereafter referred to as the average brain tissue conductivity, since it is equal to the averaged value of the conductivity of gray and white matter at 300 MHz. The conductivity of deionized water at 300 MHz is insignificant (0.002 S/m) and is considered to be zero in the calculations (25). In the computer model the coil was driven with four voltage sources with identical magnitude and phase. The voltage sources were spaced evenly about the coil.

In vivo experimental imaging and computer modeling were also performed with a human head. The 3D head model was created using images from the National Library of Medicine's Visual Human Project in a space of $62 \times$

¹Center for NMR Research, Department of Radiology, Pennsylvania State University College of Medicine, Hershey, Pennsylvania.

²Center for MR Research, Department of Radiology, School of Medicine, University of Minnesota, Minneapolis, Minnesota.

Grant sponsor: Whitaker Foundation; Grant number: RG-99-0157; Grant sponsor: NIH; Grant numbers: NS38070; NS39043; P41 RR08079; Grant sponsors: Keck Foundation; National Foundation for Functional Brain Imaging; U.S. Department of Energy.

*Correspondence to: Qing X. Yang, Center for NMR Research, NMR/MRI Building, Department of Radiology H066, Pennsylvania State University College of Medicine, 500 University Drive, Hershey, PA 17033. E-mail: qyang@psu.edu

Received 18 April 2001; revised 3 January 2002; accepted 3 January 2002.

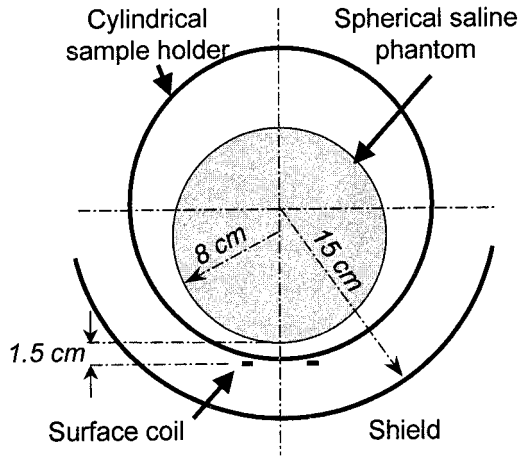


FIG. 1. Experimental configuration for the surface coil and phantom.

36×40 cm. The resolution of the model was 2.0 mm in the x and y dimensions, and 2.5 mm in the z dimension.

All numerical simulations were performed on a PC with the XFDTD program (REMCOM, Inc., State College), which uses the finite-difference time-domain method to solve Maxwell's wave equations (26,27). The image intensity calculation from the B_1 field numerical solutions has been previously described (24,28–29); therefore, only a brief description of the calculation is given below. The RF field in a sample with a high dielectric constant is elliptically polarized. The RF field interacts with magnetization through the circularly polarized components, which can be constructed on an axial plane through the center of the sample as

$$\hat{B}_1^+ = (\hat{B}_x + i\hat{B}_y) \div 2 \quad [1a]$$

$$\hat{B}_1^- = (\hat{B}_x - i\hat{B}_y)^* \div 2 \quad [1b]$$

where \hat{B}_x , \hat{B}_y , \hat{B}_1^+ , and \hat{B}_1^- are complex variables as denoted with a circumflex, $i = \sqrt{-1}$, the asterisk indicates a complex conjugate operation. The imaginary components are 90° out of phase with the real components. Assuming the component \hat{B}_1^+ is in the direction of nuclear precession, the image intensity distribution, I , due to excitation is

$$I \propto \rho \sin(V|\hat{B}_1^+|\gamma\tau) \quad [2]$$

where γ is the gyromagnetic ratio, τ is the excitation pulse duration (a rectangular pulse assumed) and ρ is spin density. The dimensionless scaling factor, V , can be considered as proportional to the coil's driving voltage in a given experiment, and thus proportional to flip angle. For reception, I is proportional to the RF field generated by the coil according to the reciprocity principle. In the low-field case, the B_1 field and its circularly polarized components B_1^+ and B_1^- can be considered as real quantities, following a simple relationship $|\hat{B}_1^+| = |\hat{B}_1^-| = \frac{1}{2}|\hat{B}_1|$. The spatial distributions of $|\hat{B}_1|$, $|\hat{B}_1^+|$, and $|\hat{B}_1^-|$ in the sample are essentially the same; therefore, using any one of these

three quantities to calculate the relative image distribution yields a valid result. In the presence of wave behavior at high fields, however, the distributions of these three quantities are significantly different. In this specific case, \hat{B}_1^- must be used to calculate the reception contribution to the image intensity. This can be understood as a result of Faraday's law that governs the reception. Thus, the image intensity can be calculated by

$$I \propto \rho \sin(V|\hat{B}_1^+|\gamma\tau)|(\hat{B}_1^-)^*|. \quad [3]$$

Note that the image intensity depends sinusoidally on $|\hat{B}_1^+|$ and linearly on $|\hat{B}_1^-|^*$. This difference in excitation and reception leads to an asymmetric image intensity distribution in the axial images when the excitation flip angle is large.

Phantom and human brain images were acquired on a 7.0 T human imaging system (Magnex magnet with Varian NMR console) using the gradient-recalled echo (GRE) method with $TR = 50\text{--}100$ ms, slice thickness = 5 mm, matrix = 128×128 , and $FOV = 24 \times 24$ cm². The coil was tuned and matched for each saline concentration. The input power level for maximum free induction decay (FID) intensity from the whole volume of the load was determined to produce the nominal 90° flip angle. The GRE images of a normal volunteer were acquired with the head placed such that the occipital lobe was roughly coaxial with the coil and the back of the head was 1.5 cm from the coil center.

RESULTS

A set of axial GRE human brain images acquired with various excitation power levels using the surface coil at 7.0 T is presented in Fig. 2a. The image intensity distribution is distinctively different from that conventionally seen in images taken with a surface coil at low fields. The most striking feature in both the experimental and calculated images is two prominent vertical dark bands on each side of the brain (see arrows), producing a "W"-shaped image intensity distribution. This image intensity distribution and its changes with RF excitation power level are predicted in the calculated images shown in Fig. 2b. The nonuniform image intensity at high field is more prominent and more frequently observed in human head images acquired with a volume coil as a hyperintense region in the center of the head (30–32). Although the appearance is different with surface and volume coils, in both cases the cause can be attributed to wave behavior. Artifacts due to wave behavior are initially observed at 3.0 T and become more prominent in images acquired at higher field strengths.

The intensity distributions in the head images in Fig. 2 are the result of the interactions between the RF field and tissues in the head. Such interactions can be described in terms of the induced conducting and displacement currents that are associated with the conductivity and permittivity of the tissue, respectively. To understand the contribution of these two components to the resultant RF field in the human body, a phantom study with variable conduc-

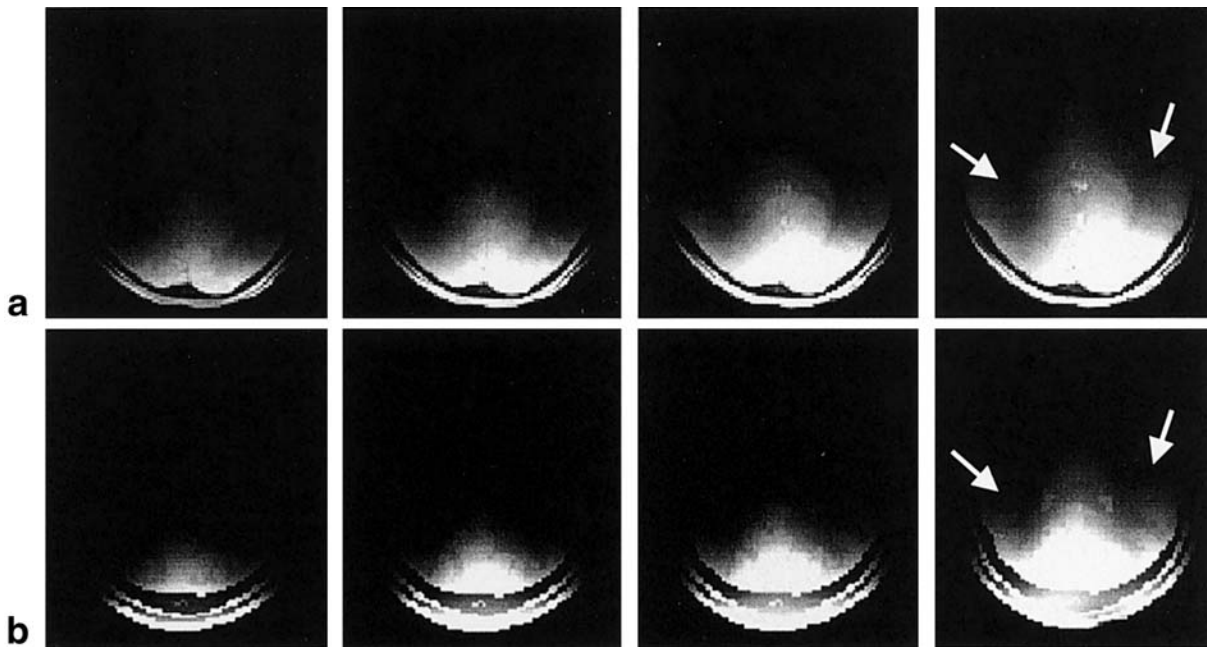


FIG. 2. (a) Axial GRE images of the brain acquired with a surface coil with various flip angles and (b) the calculated images from the numerical solutions of the B_1 field. There is a 6 dB power increment between each column from left to right. The arrows in the images indicate the dark bands on each side of the brain. The surface coil was located 1.5 cm posterior to the head.

tivity was carried out. A spherical water phantom of 16-cm diameter has a two-lobe dielectric resonance at approximately the Larmor frequency—a special situation that highlights the effects of the contribution. Figure 3 shows how the image intensity distribution on the center axial plane of the water phantom varies with sample conductivity or salinity. The plots on the bottom in Fig. 3 represent the signal intensities along the centerline in the experimental images. The calculated and experimental images are similar for all these cases. With no salinity ($\sigma = 0$), signal intensity distributions in the image and the line plot exhibit the characteristic standing-wave pattern of a second-order resonance. With increasing conductivity (salinity) the standing-wave pattern is dampened until in 150 mM saline all that remains is a monotonic decay of image intensity with increasing distance from the coil. Notice also that the maximum image intensity near the coil is significantly reduced due to decreased RF penetration in the 150-mM sample. More importantly, the minimum image intensity (nodes of standing wave) appears elevated from zero with increasing conductivity, indicating that the RF field exhibits a traveling-wave component. To further validate the observation on this wave behavior change, the instantaneous $|B_1|$ distributions at progressive points in time are calculated at 300 MHz for the deionized water ($\sigma = 0.0$ S/m), 20 mM ($\sigma = 0.26$ S/m), and 50 mM ($\sigma = 0.67$ S/m) saline (Fig. 4). The RF field in the deionized water shows clear standing-wave behavior with a time-invariant point at the center of the sphere. Therefore, the RF field in the deionized water phantom is in a resonant state, resulting in the dielectric resonance pattern in the corresponding image in Fig. 3. It is apparent that the RF field in the sample with $\sigma = 0.26$ S/m is no longer a “pure” standing wave, as the constant progression of a high-field

lobe can be followed from one side of the sample near the coil to the other. Thus, the nature of the RF field in a conductive sample is dramatically changed, exhibiting a traveling-wave characteristic. In addition to the decay with penetration into the sample, the amplitude of the traveling wave is modulated over the space by a “standing-wave envelope” (33). This effect can be seen more clearly by observing the amplitude distribution in these three different saline concentrations in Fig. 5. The node of the standing-wave pattern in the deionized water rises from zero with increasing conductivity, and then diminishes in the 50-mM saline. The corresponding amplitude plots along the centerline of the bottom row follow essentially the same trend in the experimental images in Fig. 3. The standing-wave pattern can be considered to be caused by the superposition of the progressively-attenuated transmitted and reflected waves. As the attenuation increases, there comes a point at which there is a negligible wave to be reflected, resulting in the smooth decay shown on the right of Fig. 3.

Since the geometry of the computer model of the phantom-coil configuration is precisely matched to experimental dimensions, the calculated image of the water phantom reproduces the specific intensity distribution in the experimental data remarkably well. As indicated by arrow A in Fig. 3, the image of the phantom with the averaged brain tissue conductivity shows a “W”-shaped intensity distribution similar to the brain images in Fig. 2. However, an intensity dip along the centerline in the phantom (arrow B in Fig. 3) is absent in the brain images in which the intensity drops monotonically. This difference is attributed to the difference in the relative permittivities of water and brain tissue.

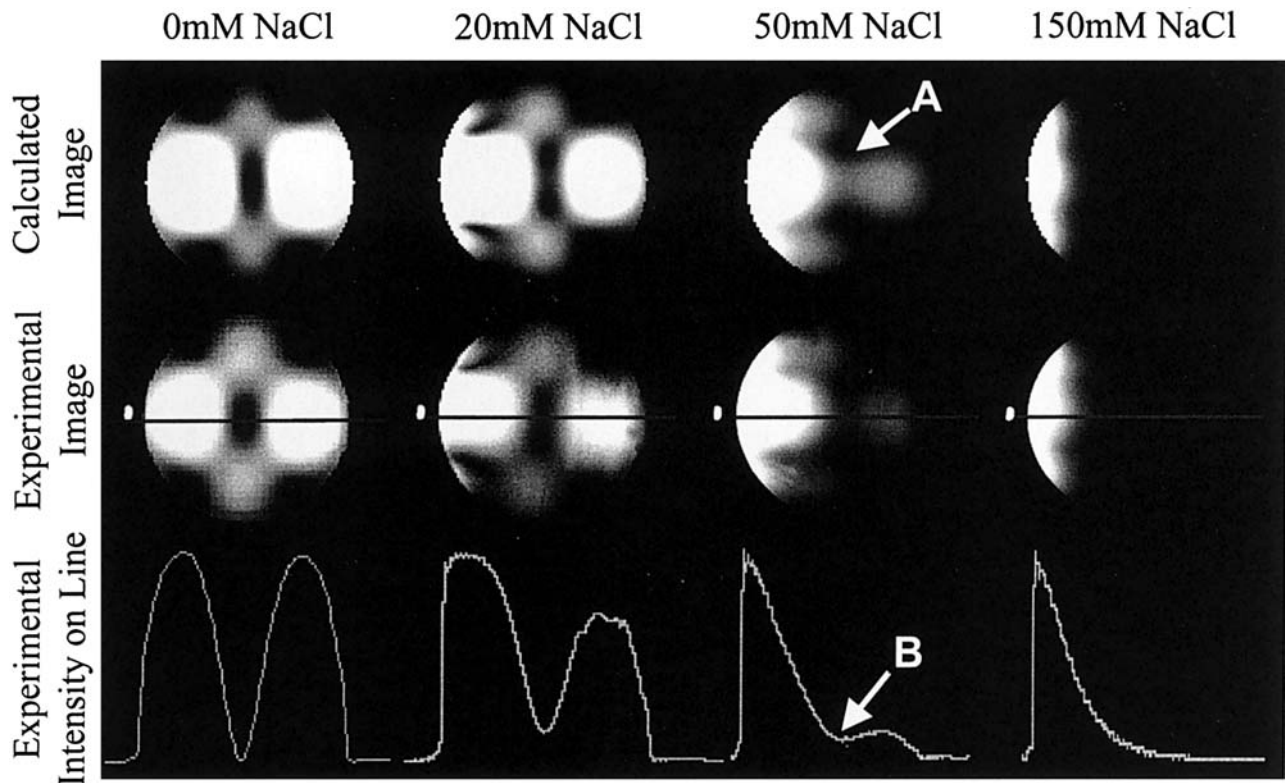


FIG. 3. The calculated and experimental axial images of phantoms with different salinity. The arrow A indicates the image intensity that resembles the “W”-shaped intensity distribution in the brain image shown in Fig. 2. Arrow B points to the image intensity dip along the centerline. This “dip” in the saline phantom image is absent in the brain image. The surface coil is on the left side of the phantom, with its position indicated by an image marker (a white dot) in each experimental image. To display clearly the spatial distribution for each sample condition, the grayscale of the image intensity distribution and the corresponding centerline plot are scaled independently for each case.

DISCUSSION

In all the cases we studied, the numerical calculations correctly predicted the experimentally-identified image intensity patterns. For phantom studies, many subtle details in the experimental images can be accurately reproduced in calculated results. For example, the signal intensities exhibit a slight asymmetry about the centerline through the phantom and coil in the images of 50- and 150-mM NaCl phantoms. As discussed in the Methods section, the asymmetry in image intensity is expected because the contributions of excitation and reception are different in forming a GRE image. The calculated result also closely reproduced the signal behavior such that the asymmetry is more apparent in the region near the coil where the flip angle is relatively larger. For human brain studies, the experimental images in Fig. 2 exhibit stronger asymmetric intensity distributions near the surface area than do the corresponding calculated images. This notable discrepancy is likely caused by the differences in anatomical structures between the human subjects used for experiment and calculation, and limited resolution of the computer model. For more detailed studies on the B_1 field near the surface of the head, a computer model with greater resolution is required in order to represent the multilayer (skin, fat, bone, etc.) anatomical structures of the human head more precisely. Nevertheless, the results clearly demonstrate the reliability and accuracy of our computer-mod-

eling method. Such valid computer models will find various applications in RF field studies and RF coil engineering, especially in high-field MRI.

Nonuniform image intensity in human and water phantom sample images at high-field strengths has been the subject of intensive investigation (13–23,29–31). In general, these distributions are due to focusing of the field, and they contain a mix of modes. However, since a resonance mode of the water phantom is close to the Larmor frequency of the 7.0 T system, a single mode is dominant and a nearly pure standing wave is formed, as demonstrated in Fig. 4. In this situation, the amplitude of the B_1 field inside the sample is stronger than that near the coil outside the sample, as shown in Fig. 5a. Such RF field behavior fits the classical resonance description of a resonance cavity, and the water phantom is a dielectric resonator. It can be easily shown with a network analyzer that there is a resonance mode near 300 MHz for the spherical water phantom used for this study, which is consistent with the results of the analytical treatment of resonance modes in a dielectric sphere (34). As the sample becomes increasingly conductive, the rapid damping of both transmitted and reflected waves prevents the formation of a stable standing wave required for a sustaining electromagnetic field resonance. Consider a simple example of a plane wave traveling through a 16-cm-thick slab of medium, with the average brain tissue conductivity

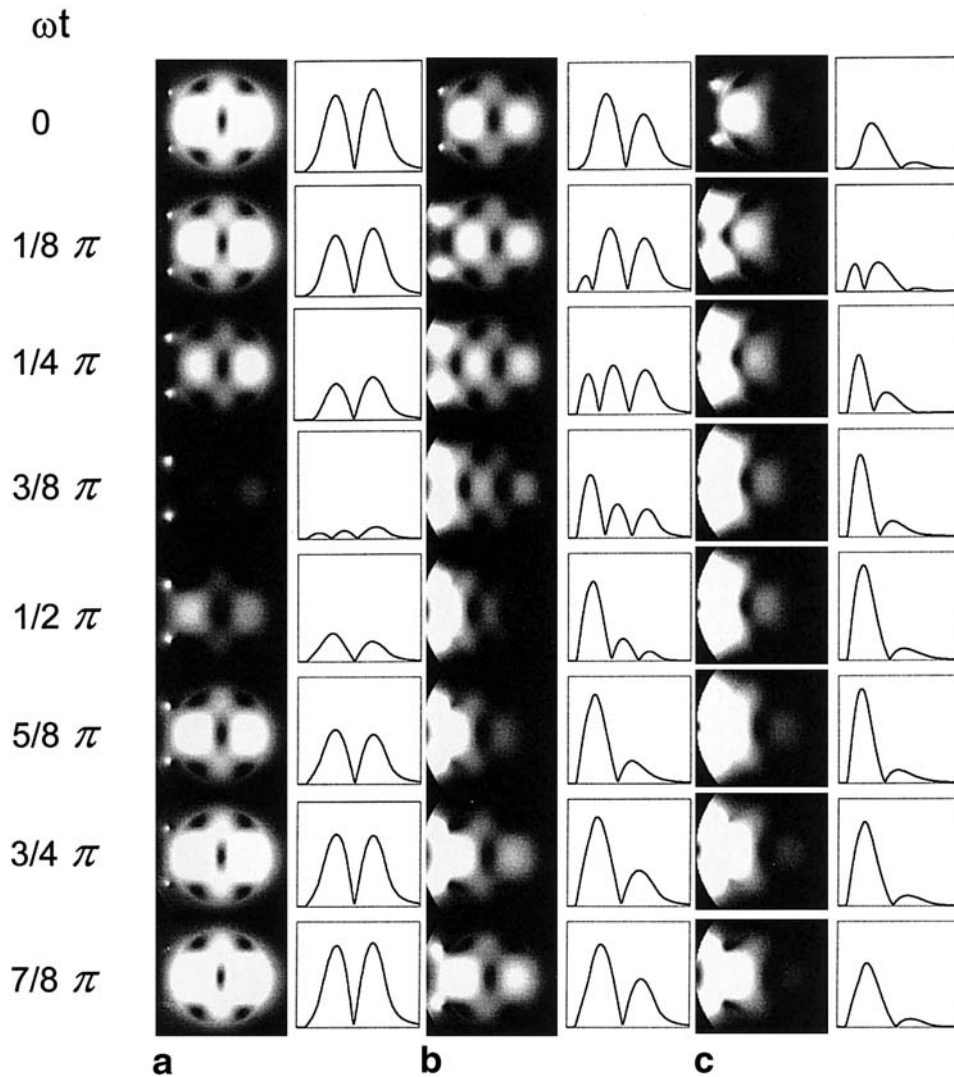


FIG. 4. The grayscale 2D plots of instantaneous transverse $|B_1|$ at progressing points during a half period in phantoms with (a) $\sigma = 0$ S/m, (b) $\sigma = 0.26$ S/m, and (c) $\sigma = 0.67$ S/m. The intensity profiles along the horizontal centerlines are also shown on the right of the 2D plots. The surface coil position is indicated by two small dots on the left side of the phantom. The relative permittivity of water ($\epsilon_r = 78$) was used in all three cases. Since the temporal B_1 strength varies greatly among these three cases, the signal intensities of temporal points are normalized individually for each conductivity condition in order to visualize the temporal change for all the conditions clearly.

($\sigma = 0.67$ S/m) and relative permittivity ($\epsilon_r = 51$) at 300 MHz. Assuming the incident wave is normal to the boundary surfaces between the medium and air, the reflectivity, Γ , is 78%. The attenuation constant, α , of the wave inside the sample can be calculated as 16 m^{-1} . The amplitude of the RF field would be reduced to 7.3% of the initial value at the entry boundary as the wave travels from one side of the slab to the other. The amplitude of the reflected wave is less than 0.5% of the initial value when it returns to the entry boundary. Under such conditions, a standing wave cannot be observed. Thus, the RF field in the human head is dominated by the traveling wave transmitted by the coil, and the field's amplitude is modulated with a specific spatial distribution over the sample. The amplitude distribution is determined by the electrical properties of the sample and boundary conditions of the sample-coil system. The observed traveling-wave behavior in the conductive sample is more analogous to that in a lossy transmission line with mismatched load impedance than in a resonant cavity. In the former case, at a general point in the sample, the magnitude of the reflected wave is smaller than that of the transmitted wave, resulting in a decaying traveling wave whose magnitude is modulated. We cau-

tion, however, that the RF field in a conductive sample in an MRI experiment is more complicated than in a mismatched transmission line because the geometry of the system is more complex. Thus, image intensity variation in a conductive dielectric sample is primarily caused by electromagnetic wave amplitude and phase interference patterns that are determined by the sample-coil configuration. In this study, with a high quality (Q) factor, the water phantom has a particular intrinsic mode at resonance near the Larmor frequency of protons at 7.0 T (34). In this case, the Q -factor is progressively dampened as the conductivity of the water increases, until eventually all evidence of the resonance disappears. Concomitantly, evidence of standing-wave behavior diminishes until, with 50 mM saline, it has vanished completely. If standing waves are no longer visible at resonance, they are unlikely to be manifested at other frequencies. This is an important conclusion of this study.

We may apply insights gathered from our phantom studies to an understanding of images obtained from humans. The available electromagnetic properties of gray and white matter are plotted in the frequency range currently available for human MRI systems in Fig. 6a (35,36). Conductiv-

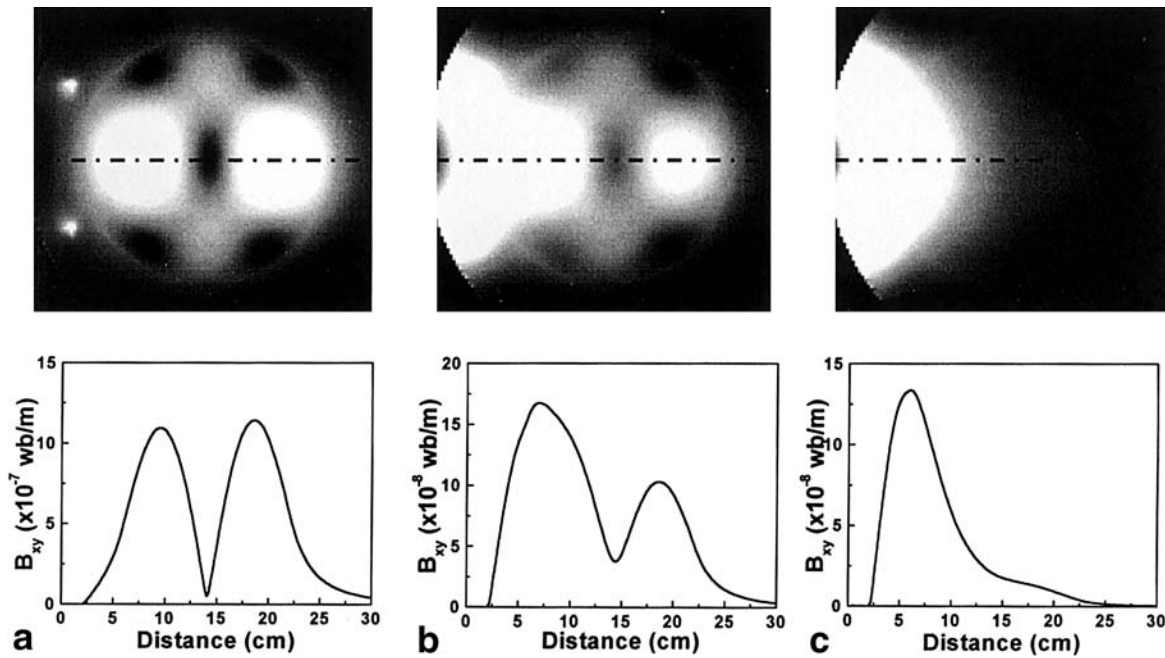


FIG. 5. The corresponding amplitude distributions of the transverse $|B_{xy}|$ field with (a) $\sigma = 0$ S/m, (b) $\sigma = 0.26$ S/m, and (c) $\sigma = 0.67$ S/m in Fig. 4. The double dotted lines in the 2D plots (top row) indicate where the line plots in the bottom row are drawn. To display clearly the spatial distribution for each sample condition, the grayscale of the transverse $|B_{xy}|$ distribution and the corresponding centerline plot are scaled independently for each case.

ity increases while the dielectric constant decreases with frequency. Their influence on the electromagnetic wave field depends on the ratio of the conducting and displacement currents: $\sigma/\omega\epsilon_0\epsilon_r$, as shown in Fig. 6b. The conducting current and displacement current in a medium are competing factors for wave propagation. Although tissue conductivity increases with frequency, the displacement current becomes more dominant as frequency increases. For averaged brain tissue, the ratio is $2.0 > \sigma/\omega\epsilon_0\epsilon_r > 0.67$ in a frequency range of 50–500 MHz. The brain tissues are neither purely dielectric (such as pure water in which $\sigma/\omega\epsilon_0\epsilon_r \ll 1$) nor purely conductive (such as metals in which $\sigma/\omega\epsilon_0\epsilon_r \gg 1$). Thus, the electromagnetic field behavior in these two extreme cases is not useful for interpreting the phenomena occurring in the human sample. Using data in Fig. 6b, the depth of penetration, $\delta = 1/\alpha$, and reflectivity, Γ , as functions of frequency, can be calculated (Fig. 6c) (33). These plots indicate that as frequency increases, electromagnetic waves decay faster in the brain, and the boundary between brain and air becomes less reflective. Therefore, it is even less likely that resonance can occur in a human head at even higher field strengths. The plots in Fig. 6d indicate that the wavelength change in brain tissue due to conductivity variation becomes less significant as field strength increases (33). In the human body, the electromagnetic properties are heterogeneous and boundary conditions are more complicated. The plots in Fig. 6 are only first-order approximations, describing the general behavior of the RF field in the human body in high-static magnetic field systems.

Although the sample-coil configuration study presented here is the simplest case, the analysis and conclusions can be generalized into more complicated cases using the prin-

ciple of superposition. For example, the RF field distribution in a birdcage or TEM volume coil can be analyzed by considering all conductor elements as individual sources with synchronized phase relationships (37). The RF field distribution in the sample is the result of the interference of the wave fields from the individual sources plus the contribution of the near fields. Thus, the hyperintense region in the center of the head in a high-field volume coil can be considered to be due to the partially-constructive superposition of RF waves transmitted from each of the conductors in the coil and reflected from the sample boundaries, plus the still-substantial near-field contributions.

CONCLUSIONS

Comparisons between experimental and calculated results under various conditions have shown that our numerical calculation method can reliably predict RF field behavior at high frequency. A temporal progression of RF field at 300 MHz can be observed using numerical calculations. The physical pictures of the RF wave field responsible for the characteristic nonuniform intensity in the high-field images of the human head and water phantoms are clearly demonstrated. A standing-wave pattern, and any associated dielectric resonances occurring in a pure water sample at specific frequencies, cannot be sustained in the human head because of the strong decay of the RF electromagnetic wave caused by sample resistance. The amplitude distribution of the fields in the head is the result of the interference pattern of decaying traveling waves in a given sample-coil configuration plus contribution from near fields. The wave behavior with respect to the electrical properties of the sample (conductivity and permittiv-

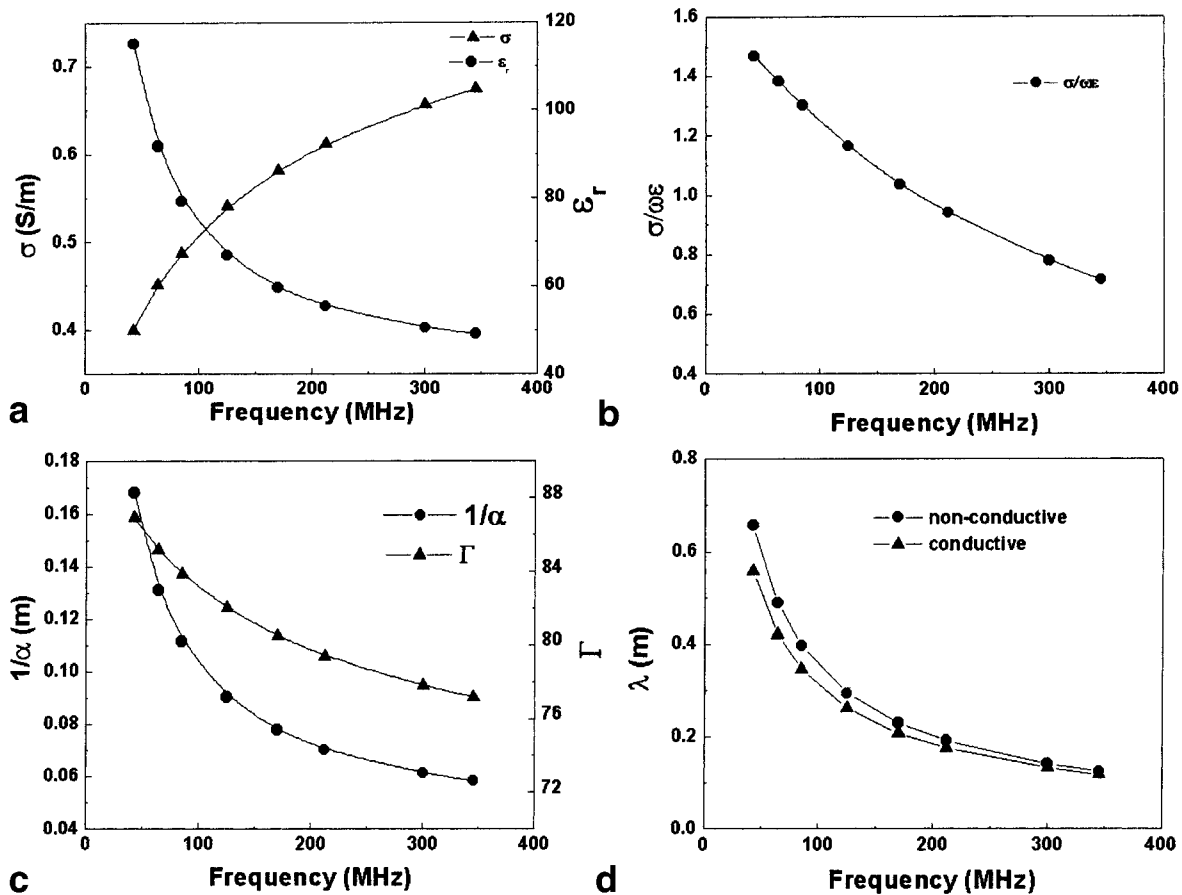


FIG. 6. (a) The frequency dependencies of the averaged conductivity and relative permittivity of brain tissue, (b) the corresponding ratio of the conducting and displacement currents, (c) the depth of penetration ($1/\alpha$) and reflectivity (Γ) at the brain tissue/air interface, and (d) the wavelength calculated with and without considering the conductivity. The values used for a were obtained from Ref. 35. A plane wave in a homogeneous medium is assumed for the plots in c. The reflectivity is valid only for the incident wave normal to the interface.

ity) is determined by the ratio of conducting and displacement currents in the sample. For a human brain tissue sample, this ratio is in a distinct regime. Large permittivity in most tissues facilitates RF wave penetration and propagation, while the conductivity of the tissue leads to a rapid decay of the RF wave, which prevents RF field penetration. The method and results presented are important for high-field MRI and RF field engineering.

ACKNOWLEDGMENTS

Contributions to the 7.0 T experimental work by Drs. H. Merkle, P. Andersen, S. Michaeli, and G. Adriany are acknowledged.

REFERENCES

- Edelstein WA, Glover GH, Hardy CJ, Redington RW. The intrinsic signal-to-noise ratio in NMR imaging. *Magn Reson Med* 1986;3:604–618.
- Ocali O, Atalar E. Ultimate intrinsic signal to noise ratio in MRI. *Magn Reson Med* 1998;39:462–473.
- Hen H, Denison TJ, Singerman RW, Balaban RS. The intrinsic signal to noise ratio in human cardiac imaging at 1.5, 3, and 4 T. *J Magn Reson* 1997;125:65–71.
- Turner R, Jezzard P, Wen H, Kwong KK, Bihan DL, Zeffiro T, Balaban RS. Functional mapping of the human visual cortex at 4 and 1.5 Tesla using deoxygenation contrast EPI. *Magn Reson Med* 1993;29:277–279.
- Ordidge RJ, Gorell JM, Deniau JC, Knight RA, Helpert JA. Assessment of relative brain iron concentrations using T_2 -weighted and T_2^* -weighted MRI at 3 Tesla. *Magn Reson Med* 1994;32:335–341.
- Yang QX, Dardzinski BJ, Li S, Smith MB. Multi-gradient echo with susceptibility inhomogeneity compensation (MGESIC): demonstration of fMRI in the olfactory cortex at 3.0 T. *Magn Reson Med* 1997;37:331–335.
- Ugurbil K, Hu X, Chen W, Zhu XH, Kim SG, Georgopoulos A. Functional mapping in the human brain using high magnetic fields. *Philos Trans R Soc Lond B Biol Sci* 1999;35:1195–213.
- Chen W, Ugurbil K. High spatial resolution functional magnetic resonance imaging at very-high-magnetic field. *Top Magn Reson Imaging* 1999;10:63–78.
- Hoult DI, Phil D. Sensitivity and power deposition in a high-field imaging experiment. *J Magn Reson Imaging* 2000;12:46–67.
- Yacoub E, Shmuel A, Pfeuffer J, Moortele P, Adriany G, Anderson P, Vaughan JT, Merkle Hellmut, Ugurbil K, Hu X. Imaging brain function in humans at 7 Tesla. *Magn Reson Med* 2001;45:588–594.
- Yang QX, Smith MB, Zhu X, Liu H, Michaeli S, Zhang X, Anderson P, Adriany G, Merkle H, Ugurbil K, Chen W. T_2^* -weighted human brain imaging with the GESEPI at 7.0 Tesla. In: Proceedings of the 8th Annual Meeting of ISMRM, Denver, 2000. p 1684.
- Robitaille PM, Abduljalil AM, Kangarlu A. Ultra high resolution imaging of the human head at 8 Tesla: 2K \times 2K for Y2K. *J Comput Assist Tomogr* 2000;24:2–8.

13. Sled JG, Pike GB. Standing wave and RF penetration artifacts caused by elliptic geometry: an electrodynamics analysis. *IEEE Trans Med Imaging* 1998;17:653–662.
14. Han Y, Wright SM. Analysis of RF penetration effects in MRI using finite-difference time-domain method. In: Proceedings of the 12th Annual Meeting of SMRM, New York, 1993. p 1327.
15. Carlson JW. Radiofrequency field propagation in conductive NMR samples. *J Magn Reson* 1988;78:563–573.
16. Tofts PS. Standing waves in uniform water phantoms. *J Magn Reson Ser B* 1994;104:001–005.
17. Foo TK, Hayes C, Kang YW. Reduction of RF penetration effects in high field imaging. *Magn Reson Med* 1992;23:287–301.
18. Keltner JR, Carlson JW, Roos MS, Wong ST, Wong TL, Buddinger TF. Electromagnetic fields of surface coil in vivo NMR at high frequencies. *Magn Reson Med* 1991;22:467–480.
19. Alsop DC, Connick TJ, Mizsei G. A spiral volume coil for improved RF field homogeneity at high static magnetic field strength. *Magn Reson Med* 1998;40:49–54.
20. Yang QX, Li CS, Smith MB. The effect of sample loading on the radio frequency magnetic field distribution in high field: contributions of dielectric resonance. In: Proceedings of the 12th Annual Meeting of SMRM, New York, 1993. p 1367.
21. Jin J, Chen J. On the SAR and field inhomogeneity of birdcage coils loaded with the human head. *Magn Reson Med* 1997;38:953–963.
22. Collins CM, Li S, Smith MB. SAR and B_1 field distributions in a heterogeneous human head model within a birdcage coil. *Magn Reson Med* 1998;40:847–856.
23. Ibrahim TS, Lee R, Baertlein BA, Robitaille PM. B_1 field homogeneity and SAR calculations for the birdcage coil. *Phys Med Biol* 2001;46:609–619.
24. Collins CM, Smith MB. Signal-to-noise ratio and absorbed power as functions of main magnetic field strength and definition of “90°” RF pulse for the head in the birdcage coil.
25. Schwan HP. Electrical properties of tissue and cell suspensions. *Adv Biol Med Phys* 1957;5:147–209.
26. Kunz KS, Luebbers RJ. The finite difference time domain method for electromagnetics. Boca Raton: CRC Press; 1993.
27. Yee KS. Numerical solution of initial boundary value problems involving Maxwell’s equations in isotropic media. *IEEE Trans Ant Propag* 1966;14:302–307.
28. Glover GH., Hayes CE, Pelc NJ, Edelstein WA, Mueller OM, Hart HR, Hardy CJ, O’Donnell M, Barber WD. Comparison of linear and circular polarization for magnetic resonance imaging. *J Magn Reson* 1985;64:255–270.
29. Hoult DI. The principle of reciprocity in signal strength calculations—a mathematical guide. *Concepts Magn Reson* 2000;4:173–187.
30. Barfuss H, Fischer H, Hentschel D, Ladebeck R, Oppelt A, Wittig R. In vivo magnetic resonance imaging and spectroscopy of human with a 4 T whole-body magnet. *NMR Biomed* 1990;3:31–45.
31. Vaughan JT, Marwood M, Collins CM, DelaBarre L, Adriany G, Andersen P, Merkle H, Smith MB, Ugurbil K. 7 T vs. 4 T: Preliminary B_1 , SNR, SAR comparison in the human head. In: Proceedings of the 8th Annual Meeting of ISMRM, Denver, 2000. p 147.
32. Kangarlu A, Baertlein BA, Lee R, Ibrahim T, Yang L, Abduljalil AM, Robitaille PM. Dielectric resonance phenomena in ultra high field MRI. *J Comput Assist Tomogr* 1999;23:821–831.
33. Johnk CT. Engineering electromagnetic fields and waves. New York: Wiley; 1988. p 363.
34. Stratton JA. Electromagnetic theory. New York: McGraw-Hill; 1941. p 554.
35. Gabriel C. Compilation of the dielectric properties of body tissues at RF and microwave frequencies. Brooks Air Force Base, TX: Air Force materiel command, AL/OE-TR-1996-0037; 1996.
36. Gabriel S, Lau RW, Gabriel C. The dielectric properties of biological tissues. III. Parametric models for the dielectric spectrum of tissues. *Phys Med Biol* 1996;41:2271–2293.
37. Vaughan JT, Hetherington HP, Otu JO, Pan JW, Pohost GM. High frequency volume coils for clinical NMR imaging and spectroscopy. *Magn Reson Med* 1994;32:206–218.